



Published in final edited form as:

*Neuroimage*. 2017 May 15; 152: 530–537. doi:10.1016/j.neuroimage.2017.03.021.

## Cerebrospinal and Interstitial Fluid Transport via the Glymphatic Pathway Modeled by Optimal Mass Transport

Vadim Ratner<sup>c</sup>, Yi Gao<sup>d</sup>, Hedok Lee<sup>a</sup>, Rena Elkin<sup>b</sup>, Maiken Nedergaard<sup>e</sup>, Helene Benveniste<sup>a</sup>, and Allen Tannenbaum<sup>b,c,\*</sup>

<sup>a</sup>Department of Anesthesiology, Yale School of Medicine, New Haven, CT, 06519, USA

<sup>b</sup>Department of Applied Mathematics and Statistics, Stony Brook University, Stony Brook, NY, 11790, USA

<sup>c</sup>Department of Computer Science, Stony Brook University, Stony Brook, NY, 11790, USA

<sup>d</sup>Department of Biomedical Informatics, Stony Brook University, Stony Brook, NY, 11790, USA

<sup>e</sup>School of Medicine, Rochester University, NY, 14642, USA

### Abstract

The glymphatic pathway is a system which facilitates continuous cerebrospinal fluid (CSF) and interstitial fluid (ISF) exchange and plays a key role in removing waste products from the rodent brain. Dysfunction of the glymphatic pathway may be implicated in the pathophysiology of Alzheimer's disease. Intriguingly, the glymphatic system is most active during deep wave sleep general anesthesia. By using paramagnetic tracers administered into CSF of rodents, we previously showed the utility of MRI in characterizing a macroscopic whole brain view of glymphatic transport but we have yet to define and visualize the specific flow patterns. Here we have applied an alternative mathematical analysis approach to a dynamic time series of MRI images acquired every 4 min over ~3 hrs in anesthetized rats, following administration of a small molecular weight paramagnetic tracer into the CSF reservoir of the cisterna magna. We use Optimal Mass Transport (OMT) to model the glymphatic flow vector field, and then analyze the flow to find the network of CSF-ISF flow channels. We use 3D visualization computational tools to visualize the OMT defined network of CSF-ISF flow channels in relation to anatomical and vascular key landmarks from the live rodent brain. The resulting OMT model of the glymphatic transport network agrees largely with the current understanding of the glymphatic transport patterns defined by dynamic contrast-enhanced MRI revealing key CSF transport pathways along the ventral surface of the brain with a trajectory towards the pineal gland, cerebellum, hypothalamus and olfactory bulb. In addition, the OMT analysis also revealed some interesting previously unnoticed behaviors regarding CSF transport involving parenchymal streamlines moving from ventral reservoirs towards the surface of the brain, olfactory bulb and large central veins.

\*Corresponding author at: Department of Computers Science and Applied Mathematics/Statistics, Stony Brook University, Stony Brook, NY 11790, USA, arobertan@gmail.com (Allen Tannenbaum).

## Keywords

Cerebrospinal fluid transport; Glymphatic transport; Liquid flow modeling; Optical flow; Optimal mass transport; Rat brain

---

## 1. Introduction

In this paper, we describe a mathematical model of the glymphatic transport system using the theory of optimal mass transport (OMT) (Mueller et al., 2013; Villani, 2008, 2003). Cerebrospinal fluid (CSF) is continuously produced in the choroid plexus of the ventricles and transported into and out of the brain in part via the glymphatic pathway (Nedergaard, 2013), a process which also facilitates removal of toxic waste proteins (Nedergaard, 2013; Iliff et al., 2012, 2013b). Notably, soluble amyloid beta ( $A\beta$ ) oligomers and tau protein have been shown to clear via the glymphatic pathway (Iliff et al., 2012; Lee et al., 2015) and it has been hypothesized therefore that dysfunction of glymphatic transport underlie buildup of extracellular  $A\beta$  aggregates and tau as seen in Alzheimer's disease. The anatomical structure of the glymphatic pathway is complex but a key component is the peri-vascular compartment. The outer perimeter of the perivascular space is defined by glial endfeet with high expression of aquaporin 4 water channels that enhances CSF transport into the interstitial fluid (ISF) space which result in exchange and clearance of waste solutes via conduits that include the peri-venous compartment (Fig. 1). Glymphatic transport of fluid and solutes is convectively driven by vascular pulsations (Iliff et al., 2013b) and by a pressure gradient over the cerebral convexity (so-called 'transmantle' pressure gradient) which can be manipulated, even by minor physiological alterations such as shifting body posture (Lee et al., 2015).

The discovery of the glymphatic pathway was based on fluorescently tagged optical dyes of different molecular weights (MW) administered into CSF in combination with *in vivo* two photon microscopy (Iliff et al., 2012; Kress et al., 2014; Xie et al., 2013). This technique allowed for dynamic characterization of the fast peri-arterial influx of optical tracers in small cortical areas of live rodents (Iliff et al., 2012). Importantly, intraparenchymal injections of miniscule amounts of soluble radiolabeled  $A\beta$  showed that  $A\beta$  cleared along the perivascular space of large central veins. It was also discovered that astrocytes play a pivotal role in linking the peri-arterial inflow and the peri-venous efflux pathways (Iliff et al., 2012).

In the present work, we derive and analyze flow patterns of the CSF based on an optical flow model derived from optimal mass transport. Preliminary results on this topic have been reported in our previous work (Ratner et al., 2015). Our novel analysis techniques including the streamlines and pathways algorithms will be explicated in Section 5 below. The mathematical theory even allows a short extrapolation in time.

We now summarize the content of this paper. In Section 2, we describe some of the background on the glymphatic pathway, and the imaging methodology used to generate the data. Section 3 is devoted to the optical flow methodology based on the theory of optimal mass transport. It includes some details about the numerical techniques we employed in generating our flow data. Next in Section 4, we sketch our experimental procedures that we

used in carrying out the specific results described in Section 5. Finally, in Section 6, we discuss the conclusions that may be drawn from the present work as well as possible future research directions.

## 2. Glymphatic Pathway Captured by MRI

The limited field-of-view of two-photon optical *in vivo* imaging prohibits visualization of the dynamic ‘macroscopic’ glymphatic process at a systems level. Therefore, to translate the glymphatic pathway findings observed with optical imaging towards a dynamic test-bed allowing for analysis of the whole rodent brain, injection of paramagnetic contrast molecules into CSF of rat brain was combined with dynamic T1-weighted 3D brain MRI on a 9.4T microMRI instrument (Iloff et al., 2013a). We used gadolinium diethylenetriamine-pentaacetic acid (Gd-DTPA, MW 938 Da, 1:40 dilution in sterile water, 12.5 mM, isobaric with CSF) administered into the cisterna magna of rats (Iloff et al., 2013a). A key assumption with this approach was that Gd-DTPA behaves as a surrogate waste ‘solute’ in CSF and further that its presence does not perturb normal brain physiology. A series of T1 weighted 3D MRIs of the rat brain visualized in real time revealed how the Gd-DTPA molecules moved into the rat brain, first along the large arteries at the base of the brain and then slowly (over 2 – 4 hrs) penetrated into the brain parenchyma where it redistributed and slowly cleared via peri-venous routes and along cranial nerves. Fluorescently tagged dyes injected into CSF using the same experimental set-up validated the glymphatic transport of Gd-DTPA (Iloff et al., 2013a). Quantification of glymphatic transport of Gd-DTPA was accomplished using both parametric ROI analysis as well as non-parametric cluster analysis (Iloff et al., 2013a). Another recent study extended this analysis to include 2-compartment modeling where ‘retention’ and clearance of a given tracer was calculated over a finite period of time from whole brain (Lee et al., 2015).

Fig. 2 illustrates how glymphatic transport of the CSF paramagnetic tracer, Gd-DTPA was previously quantified by contrast enhanced MRI. At early times after Gd-DTPA administration into CSF, contrast is most prevalent along large arteries at the base of the brain (Iloff et al., 2013a). In the rodent brain, relative rapid glymphatic inflow occurs at the level of the pons, hypothalamus, olfactory bulb, and the cerebellum (Fig. 2). For anatomical orientation, the color coded map of contrast distribution is displayed on a volume rendered surface mask of the whole rat brain and different brain regions including the cerebellum, hippocampus, superior colliculus, thalamus, hypothalamus, caudate, pons and medulla oblongata (Fig. 2). Red and blue colors represent high and low contrast, respectively. The contrast uptake into brain parenchyma is evident as a slow penetrating gradient moving from the ventral surface of the brain, towards central and olfactory areas of the rat brain; and has been validated by optical imaging (Iloff et al., 2013a).

For the quantification and visualization of the spatial-temporal characterization of contrast enhancement over time, we reported glymphatic transport of Gd-DTPA as ‘% signal change from baseline’ calculated based on pre- and post-contrast image intensities, here referred to as the ‘conventional approach’. This approach is lacking in providing information on the direction of the flow and it remains elusive as to whether parenchymal penetration is collectively a random distribution in space or if there are preferential directions in the flows.

We therefore employed OMT to extract the transport fluxes. Clearly, a mathematical model of glymphatic transport based on the underlying physics of fluid flow will be valuable to spatially and dynamically understand how CSF transport of ‘solutes’ is influenced by various physiological states as well as during disease.

We will sketch the mathematics of OMT in the next sections, and use this to derive an analytic model of the macroscopic view of transport through the *glymphatic system* based on fluid flow physics and brain physiology, and then test our model based on a dynamic series of contrast-enhanced MRI images.

### 3. Optimal Mass Transport (OMT)

#### 3.1. Assumptions about the Data

As briefly mentioned above, the data is collected as a time series of T1-weighted MRI images taken during and after slow administration of Gd-DTPA into CSF (cisterna magna) of an anesthetized rat (Iloff et al., 2013a; Lee et al., 2015). Before we get into the details of our model and the OMT framework behind it, we address three assumptions that we implemented in regards to the data. First (*assumption 1*), we assume that the tracer travels along the glymphatic pathway and second (*assumption 2*), we assume that the total mass of the tracer in the brain is preserved from frame to frame. Lastly, we currently assume (*assumption 3*) that the relation between tracer concentration and image brightness is linear.

We now briefly justify these assumptions. First, assumption 1 can be justified by evidence that the tracer is transported from CSF into the brain in a characteristic anatomical pattern consistent with a trajectory over time through the glymphatic pathway (Fig. 2, Iliff et al., 2012). The second assumption was made as a means to simplify the optical flow estimation. In regards to assumption 3, all the 3D T1 weighted images were acquired using a spoiled gradient echo sequence. In an ideal condition, detected MR signals (Tofts, 2005) are expected to follow the equation

$$S = \frac{S_0 \sin \theta (1 - e^{-TR/T1})}{1 - \cos \theta e^{-TR/T1}} \quad (1)$$

where T1, longitudinal relaxation time, shortens during the contrast enhancement. Using equation (1), “% signal change from baseline” was simulated as a function of contrast concentration (Fig. 3). The relaxivity of Gd-DTPA was assumed to be  $3.1 \text{ mM}^{-1} \text{ s}^{-1}$  (De Sousa et al., 2008), TR=15ms, flip angle (theta)=15°, and tissue T1=2000ms (De Graaf et al., 2001).

As seen from Fig. 3, a linear trend is discernible at a concentration below 0.15mM. From our previous study, we know that the % signal change from baseline reached over time is in the order of 70 – 80% (Iloff et al., 2013b), therefore the postulated assumption 3, pertaining to linearity between the brightness and the concentration is reasonable. In future work, we are

planning a much more detailed description implementing the actual quantification of Gd-DTPA in the brain based on T1 mapping.

### 3.2. Optical Mass Transport

We use a version of optical flow based on the theory of optimal mass transport (OMT) (Mueller et al., 2013; Villani, 2008, 2003; Haker et al., 2004), the so-called Monge-Kantorovich problem. As described in such standard references, Horn and Schunk (1981) and Lucas et al. (1981), optical flow may be considered as the apparent motion of brightness patterns in a temporal sequence of intensity images. In our case, the images are given by T1-weighted MR data. As we will explicate below, the idea is to interpret intensity as mass, and thus apply the OMT technique. We will therefore outline Monge-Kantorovich theory (Villani, 2008, 2003; Angenent et al., 2003; Evans, 1997), and then in the next section make the connection with optical flow. We should also note that an OMT formulation of optical flow was used in Mueller et al. (2013) for flame tracking.

We let  $\Omega_0$  and  $\Omega_1$  denote two convex subdomains of  $\mathbb{R}^d$ , having smooth boundaries, each equipped with a positive density function,  $\mu_0$  and  $\mu_1$ , respectively. We assume that total mass is the same, and without loss of generality this may be taken to be 1, that is

$$\int_{\Omega_0} \mu_0 = \int_{\Omega_1} \mu_1 = 1.$$

This means that  $\mu_0$  and  $\mu_1$  are probability densities (pdfs). Let  $\psi: \Omega_0 \rightarrow \Omega_1$  be a diffeomorphism which satisfies the following *Jacobian equation*:

$$\mu_0 = |\nabla \psi| \mu_1 \circ \psi. \quad (2)$$

Note that  $|\nabla \psi|$  denotes the determinant of the Jacobian.

Considering the change of variables formula, the mapping  $\psi$  is *mass preserving* (MP); see Villani (2008) for details. Equation (2) has many solutions and we denote the set of all such solutions (mass preserving mappings) as *MP*. A mapping in *MP* may be regarded as redistributing the mass of a given material (e.g. gas) with a certain pdf  $\mu_0$  to another pdf given by  $\mu_1$ .

Considering the displacement defined by  $\psi$ , we can define the following *Wasserstein metric* on pdfs:

$$d_2(\mu_0, \mu_1)^2 := \inf_{\psi \in \text{MP}} \int \|\psi(x) - x\|^2 \mu_0(x) dx. \quad (3)$$

This metric has many remarkable properties, and in fact, defines a Riemannian metric on the space of probability distributions (Otto, 2001; Villani, 2008). For our purposes, we note that

there is a unique optimal solution of (3),  $\psi_{MK}$ , which is the gradient of a strictly convex function  $g_{MK}$  (Villani, 2008, 2003; Evans, 1997). We will discuss this further in the next section, when we describe the connection of OMT to optical flow.

There are a number of ways to compute  $\psi_{MK}$ . We have followed an approach inspired by the pde based formulation given in Rachev and Rüschendorf (1998) and Angenent et al. (2003), and explicitly numerically implemented in Haber et al. (2010). This will be sketched in Section 3.4 below.

### 3.3. OMT Based Optical Flow

In this section, we review the connection of optimal mass transport theory to the computation of optical flow. This is based on some elegant work of Benamou and Brenier (2000). The idea is that the  $L^2$  Monge-Kantorovich problem may also be given an optimal control formulation in the following manner. Consider the following optimization problem:

$$\inf \int_{\mathbb{R}^d} \int_0^1 \mu(t, x) \|\nabla g(t, x)\|^2 dt dx \quad (4)$$

where the infimum is taken over all time varying densities  $\mu$  and functions  $g$  satisfying

$$\frac{\partial \mu}{\partial t} + \nabla \cdot (\mu \nabla g) = 0, \quad (5)$$

$$\mu(0, x) = \mu_0(x), \quad \mu(1, x) = \mu_1(x). \quad (6)$$

The functional (4) is the kinetic energy while  $u = \nabla g$  represents velocity. Equation (5) is the *continuity equation* enforcing the mass preservation property of the flow. One may show that the infimum of (4) is attained for some  $\mu_{min}$  and  $g_{min}$ . We set  $u_{min} = \nabla g_{min}$ . Further, the flow  $X = X(x, t)$  (written in Lagrangian coordinates) corresponding to the minimizing velocity field  $u_{min}$  defined by  $X(x, 0) = x$ ,  $X_t = u_{min}(X(x, t), t)$  is given simply as  $X(x, t) = x + t(\psi_{MK}(x) - x)$ , where  $\psi_{MK}$  is the optimal transport map described in the previous section. Note that when  $t = 0$ ,  $X$  is the identity map and when  $t = 1$ , it is the solution  $\psi_{MK}$  to the Monge-Kantorovich problem. The infimum of (4) under the constraints (5) and (6) is exactly the Wasserstein distance  $d_2(\mu_0, \mu_1)$  between  $\mu_0$  and  $\mu_1$ ; see Benamou and Brenier (2000).

This analysis provides appropriate justification for using optimal mass transport as a method for computing optimal flow when the densities  $\mu_0$  and  $\mu_1$  are interpreted as image intensities.

### 3.4. Numerical Implementation of Optimal Mass Transport

We followed the method described by Haber et al. (2010) in numerically implementing the optimal flow procedure. To discretize the optical flow equation we used the leapfrog method, which is second order accurate in space-time. In this case, the densities  $\mu(t, x)$

correspond to the image intensities  $I(t, x)$ . For simplicity, we carry this out in the plane. Note that  $x = (x_1, x_2)$ . Consider three images out of the sequence. We note  $I_{ij}^k$  as the pixel at location  $(i, j)$  at time frame  $k$ . We also denote the components of  $u = \nabla g$  as  $u_1$  and  $u_2$ . Then, the leapfrog method reads

$$I_{ij}^{k+1} - I_{ij}^{k-1} = \rho \left( (u_1 I)_{i+1,j}^k - (u_1 I)_{i-1,j}^k + (u_2 I)_{i,j+1}^k - (u_2 I)_{i,j-1}^k \right) \quad (7)$$

where  $\rho = \delta t / \delta x$ . This can be written in matrix form as

$$A_1(I)u_1 + A_2(I)u_2 = b$$

where  $b$  is the left hand side of (7) and the matrix  $[A_1(I) A_2(I)]$  is the discrete  $\nabla \cdot I(\cdot)$  operator. To discretize the integral, we use the trapezoidal method. Using the discretized quantities, we obtain a discrete analog of the optimization problem. This leads to a simple quadratic problem that can be solved using standard sequential quadratic programming methods. See Haber et al. (2010) for the details.

## 4. Experimental Animal and MRI Procedures

### 4.1. Anesthesia and Surgical Procedures

All animal procedures were approved by the Institutional Animal Care and Use Committee. Six Fisher 344 female rats were used for all studies. The rats were initially anesthetized with 3% isoflurane delivered in O<sub>2</sub> and allowed to breathe spontaneously and anesthesia was maintained with 1.7 – 2.5% isoflurane. When a surgical plane of anesthesia was achieved the rats were positioned prone in a stereotaxic frame and a CSF catheter was implanted into the cisterna magna as previously described (Lee et al., 2015). Following the implantation of the CSF catheter, the rats were prepared for MRI imaging.

### 4.2. MRI Procedures

All MRI acquisitions were performed on a 9.4T/30 magnetic resonance imaging instrument interfaced to a Bruker Avance console controlled by Paravision 6.0 software (Bruker Bio Spin, Billerica, MA, USA). Rats were scanned in a supine position using a custom-built animal cradle system. Physiological parameters, including respiratory rate, oxygen saturation, body temperature, and heart rate were continuously monitored using MRI compatible monitoring system (SA Instruments, Stony Brook, NY, USA) and kept body temperature within a range of 36.5°C–37.5°C using a heated watered. Anesthesia during MRI imaging was switched from isoflurane to dexmedetomidine. Specifically, 0.015 mg/kg of dexmedetomidine was administered i.p.  $\times 2$  followed by a continuous infusion of (0.015 – 0.020 mg/kg/hr) delivered via a subcutaneous catheter placed in the flank area. The isoflurane concentration was gradually reduced and maintained at 0.8 – 1.0% delivered in a 1:1 mixture of air:O<sub>2</sub> via a nose cone. A 2-cm planar surface radio-frequency coil (Bruker) with a built-in pre-amplifier was used as a receiver and an 86 mm diameter volume coil

(Bruker) was used as a transmitter. Following scout images, spoiled gradient echo FLASH 3D images were acquired (TR = 15 ms, TE = 4.1 ms, NEX = 1) every 4 min. Images were interpolated from  $256 \times 128 \times 128$  to  $256 \times 256 \times 256$  yielding a spatial resolution of  $0.12\text{mm} \times 0.12\text{mm} \times 0.13\text{mm}$ . The first three images were taken as a baseline and Gd-DTPA contrast infusion was started at the beginning of the fourth image. A 1 : 40 (Gd-DTPA:H<sub>2</sub>O) dilution was infused at a rate of  $1.6\mu\text{l}/\text{min}$  for a total volume of  $20\mu\text{l}$ . FLASH 3D images were acquired continuously for at least 160 minutes, totaling more than 40 frames in each study. A 2D time of flight MR angiography (MRA) sequences (TR=12ms TE=2.7ms NEX=4) was also taken at the end of the study with a spatial image resolution of  $0.12\text{mm} \times 0.12\text{mm} \times 0.20\text{mm}$  ( $256 \times 256 \times 105$ ). Translation and orientation of the 2D MRA were adjusted so that both MRA and FLASH3D images are spatially co-registered.

#### 4.3. MR Post-Processing before OMT Analysis

MRI image processing steps have been described in detail previously (Lee et al., 2015). Briefly, all images were exported in DICOM and converted into nifti file format to correct for head motion, intensity normalization across the time series, and spatial smoothing. As shown in Fig. 4A, B, changes in image contrast over time is interpreted as influx and efflux of the Gd-DTPA contrast agent. After spatial smoothing, % signal changes from the baseline, termed ‘conventional analysis’ was also calculated in each voxel as described previously (Iloff et al., 2012). MRA was also reformatted to match the spatial resolution of the FLASH3D for visualizing influx and efflux.

## 5. Experimental Results

### 5.1. Flow Pattern OMT Analysis

The flow derived from the equations in Section 3 is a vector field  $\phi$  over a 4D domain  $(x, y, z, t)$ . Such an entity is very difficult to present visually, let alone analyze. It would therefore be beneficial to present meaningful patterns in the flow that do not require the visualization of such large data. Our hypothesis is that the CSF initially flows through main channels, or “inflow pathways”, then disperses through the brain parenchyma, and then collects in specific “outflow pathways” before ultimately leaving the brain. It is important to note that this hypothesis affects neither the flow calculation, nor its analysis. As we expected, the flows from our analysis demonstrated this same behavior. It is our goal in this report to identify mainly the inflow pathways in a live rodent brain.

Let us define a streamline as a trajectory of a single particle carried by the CSF along the flow field computed in the previous section. Specifically, a set of points  $P \subset \mathbb{R}^3$  is sampled from the brain region with uniform distribution. Then, for each point  $p_i \in P$ , an ordinary differential equation is solved to compute the streamline curve  $C_i$  as:

$$\frac{dC_i}{dt} = \phi(x, y, z, t)$$

with the initial condition  $C_i(0) = p_i$

Once the streamlines are computed, we then define a pathway as a region where the number of confluent streamlines exceeds a predefined threshold. Fig. 5 is an example of the presentation of inflow pathways characterized by high streamline density; in which the direction of the physical flow of ‘mass’ and CSF is visualized moving from the red ‘origins’ of the streamlines towards their blue ‘ends’.

Let us then observe many such streamlines, sampled uniformly throughout the brain at a given time step. As seen from Figs. 4C, D, the streamlines originate from a network of inflow pathways, and are dispersed inhomogeneously throughout the brain. Areas of origin of the flow are therefore characterized by high density of streamlines, compared to the rest of the brain. It is also important to address the issue of stability of streamline computation. Since a streamline is a trajectory of a (weightless) particle carried by the CSF, its computation is straightforward: Given a vector field and a starting point, we backtrack towards its point of origin: the next point is derived by following the direction opposite to that defined by the vector field at the starting point, for a given distance (usually short). The process is then repeated for a predefined number of points. This process, as we may notice, is only stable (i.e. small changes in the starting point do not cause large changes in the trajectory) when the flow vector field diverges (i.e. the inverse vector field converges), or originates at a single source. As we can see in Figs. 4 and 5, this is indeed the case, which validates our hypothesis on the nature of the flow.

## 5.2. Anatomical Glymphatic Influx Transport by OMT Pathways

We characterized the pattern of pathways defined by OMT in 6 different rat brains. Fig. 5 shows the result of this analysis in 3 rats and demonstrates that the influx trajectories are very consistent from rat to rat (this was true for all of the rats analyzed). Specifically, at early times (first 20 – 40 min after contrast infusion) we observe the high density of ‘mass’ or reservoirs along the ventral surface of the brain from where smaller connected trajectories originate. The streamlines appear in a pattern where the end of the streamline points towards the surface of the brain. At later time points, the larger reservoirs are translocated toward the pineal recess and along the olfactory sinus (Figs. 5 and 6). These CSF reservoirs as displayed by OMT pathways are consistent with previous reports on anatomical localization of contrast after CSF injection in the rat brain (Lee et al., 2015; Iliff et al., 2013a). Fig. 6 illustrates this in 2D and shows the color coded pathways overlaid on a T1-weighted anatomical rat brain template. The pathways largely confirms previous described contrast flow (Lee et al., 2015; Iliff et al., 2013a; Jiang et al., 2016) but adds additional information. The OMT provides new information by showing that reservoirs of CSF tagged with contrast moves in specific trajectories within the brain tissue. It appears that trajectories from the larger pathway reservoirs feed smaller streams that collect in brain tissue in specific patterns - towards the olfactory bulb and surface of the brain.

## 5.3. Influx Pathways in Relation to Large Vasculature

Fig. 7 shows the pathways in relation to large cerebral vessels. The MRA of the rat brain is shown in three orthogonal planes overlaid on the corresponding anatomical T1-weighted MRI template. Several large arteries can be identified including the azygos of the anterior cerebral artery (azACA), olfactory artery (OA), middle cerebral artery (MCA), and basal

artery (BA). The large veins and sinuses are also evident such as the superior sagittal sinus (SSS), transverse sinus (TS), supraorbital vein (Sov), and cavernous sinus (Cav S). It is clear from Fig. 7 that the large pathways representing high density streamlines follow the trajectory of the large arteries on the ventral surface of the brain; and further, that additional large pathway reservoirs from the pineal recess extend towards large veins including the Galeno vein and the inferior sagittal sinus (cf. Fig. 7B).

## 6. Conclusions and Further Research

MRI is an *in vivo* imaging modality that captures the whole brain spatial-temporal characteristics of the solute transport, which may not be attainable in imaging techniques that record the state of the transport at only a single time point *ex vivo*. Underlying the transport mechanism is an inherent time dependence where influx, clearance, and distribution of solutes are all occurring simultaneously. Therefore, time and spatially resolved data provide superior understanding of where and how much solute collectively travels over time. In this paper, data were analyzed using the optimal mass transport algorithm to visualize the direction of the flow. The method successfully captured known bulk flow patterns as well as parenchymal flow fields showing coherent directionality that had not been reported previously, and may ultimately indicate the direction of clearance routes.

More specifically, we applied an optical flow model based on OMT (Monge-Kantorovich problem) to a dynamic series of contrast-enhanced MRI data from live rodent brains and mathematically derived glymphatic (tracer) flow trajectories. The computational algorithms we developed enabled visualization of the glymphatic flow patterns in the live rodent brain in relation to anatomical and vascular key landmarks and was extended to test the stability of this transport process pattern in a group of rats. Specifically, we used the OMT approach to model the glymphatic flow vector field, and then analyzed the flow to define the network of CSF flow channels or rather ‘pathways’ which appear during the time period where contrast influx from the main CSF reservoir (cisterna Magana) into the brain tissue is overriding (Fig. 2). For validation purposes it is important to point out that the OMT analysis provides similar information as the conventional analysis in regards to influx patterns but also adds new, supplementary information on ‘mass’ (contrast) transfer. Accordingly, at early time points, the OMT pathways show strong mass transfer along the base of the brain in areas associated with the large arteries including the basal artery, circle of Willis and olfactory artery similar to the conventional analysis (Lee et al., 2015; Iliff et al., 2013a; Jiang et al., 2016). However, parenchymal ‘streams’ of mass transfer from the base of the brain towards the surface of the brain and towards the olfactory bulb is evident only on the OMT processed brains and not on the conventional analysis. The OMT analysis is further informative by showing strong stream lines in brain areas associated with large veins (Fig. 7) which has also been reported in optical imaging studies (Iliff et al., 2012; Kress et al., 2014). This is very promising given that mass / solute clearance from the brain is in part occurring along perivenous spaces (Nedergaard, 2013). Although the OMT analysis is slightly different between the individual rats they all show the same trend i.e. at early times (first 20 – 40 min) there is strong mass transfer along large arteries at the base of the brain and in the cleft between the cerebellum and forebrain where large arteries are also present.

It is tempting to speculate how the OMT analysis and findings reported here may inform future pre-clinical and clinical research findings pertaining to neurodegeneration including classical small vessel disease (SVD), AD and cerebral amyloid angiopathy (CAA). For example, abnormalities pertaining to the peri-vascular space has been viewed as a common pathophysiological pathway in many neurodegenerative diseases regardless of it being primarily vascular (e.g. SVD (Wardlaw et al., 2013; Zhu et al., 2010) and CAA) and/or AD. The OMT analysis approach would permit an investigation into parenchymal CSF influx and clearance in distinct different pathologies. Hypothetically, vascular amyloid deposition (CAA) and SVD might primarily impair influx whereas parenchymal A $\beta$  aggregates (hallmark of AD) would impair parenchymal transport.

The results pertaining to peri-vascular location of pathways presented here are supported by several reports in the literature including elegant and recent work by Bedussi et al. (2016). In this paper, the distribution pattern of a high molecular weight fluorescent tracer distribution from the cisterna magna and into CSF and the perivascular compartment was characterized using a combination of imaging tools including confocal microscopy, light and electron microscopy (Bedussi et al., 2016). For this particular tracer the transport pathways were described to spread from the CM into the subarachnoid space on the ventral side of the brain in particular and along the ‘deep clefts between the major brain structures that connect the cerebral cisterns’ similar to OMT data described here. Bedussi et al. (2016) did not observe parenchymal spread of the tracer due the high MW of the tracer used (500 kDa).

Importantly, we here confirm with OMT that the tracer distributes around arteries as well as veins. In this context it is important to stress that the data and results presented here address mass transport in relation to large-caliber vasculature. The spatial resolution of the MRI data does not allow analysis at the microscopic scale, and therefore does not directly address mass transport associated with the microcirculation. This is important given the controversy regarding the direction of clearance routes in studies where solutes including amyloid beta are administered directly into the parenchyma and in some studies, show clearance along the capillaries and arterioles (Carare et al., 2008; reviewed by Bakker et al., 2016) and in others, along central veins (Iliff et al., 2012).

The parenchymal pathways and streamlines that are evident only by the OMT analysis provide new information pertaining to glymphatic transport. In previous work where contrast agents have been administered into the CSF (cisterna magna), parenchymal contrast uptake has been appreciated as a slow moving ‘barrier’ moving from the ventral surface and from the pineal recess into the tissue (Iliff et al., 2013a). Although, well-defined smaller conduits have been noted in certain locations such as along smaller arterial branches that penetrate into the brain; the pattern of well-defined streamlines penetrating the entire brain from larger reservoirs from the base of the brain towards the surface and larger venous structures have never before been appreciated using MRI based approaches. It is necessary to further validate the pathways as defined by OMT analysis to ascertain that they are truly a biological phenomenon related to the glymphatic transport process and not merely projections derived from the applied processing algorithms. Assuming that streamlines and larger pathway reservoirs are indeed ‘real’ biological entities, it is particularly intriguing that the streamlines may not be homogeneously distributed, suggesting that specific areas may be more accessible for transport of the paramagnetic tracer. Such areas may be more accessible

for solute transport due to superior convective flow streams (secondary to transmante pressure gradients) (Bakker et al., 2016) and/or location of certain outflow pathways such as the large central veins. It is also important to note that the rats in this study were anesthetized and this increases glymphatic transport efficiency when compared to wakefulness (Xie et al., 2013) and it is possible that parenchymal CSF streamlines as observed by the OMT analysis would be obliterated in awake animals. Clearly, more studies will be needed to further understand the underlying physiology governing the streamlines/pathways. Interestingly, Oreškovi and Klarica (2010) suggested a new look at CSF transport and proposed that the classical “circulation” term of CSF should be replaced by “movement” given data demonstrating multi-directional parenchymal transport of CSF.

Nevertheless, despite its simplicity, the proposed OMT model mimics the real data closely, with some errors arising from the difficulty of the inverse problem. There are a number of new directions that we plan to explore in future research. A key element would be to consider weakening the constraint of mass preservation. One direction would be to apply the approach of Benamou (2003). The idea is to combine  $L^2$  optimization with OMT in case of unbalanced mass distributions. Briefly, given two unbalanced densities  $\mu_0$  and  $\mu_1$ , one seeks a distribution  $\tilde{\mu}_1$ , the closest density to  $\mu_1$  in the  $L^2$  sense, which minimizes the Wasserstein distance  $d_2(\mu_0, \tilde{\mu}_1)$ . Other possibilities include changing the continuity equation (5) by adding a diffusion term; see (Chen et al., 2016) and the references therein.

## Acknowledgments

This research was partially supported by the National Center for Research Resources under Grant P41-RR-013218, the National Institute of Biomedical Imaging and Bioengineering under Grant P41-EB-015902 of the National Institutes of Health through the Neuroanalysis Center of Brigham and Women's Hospital, National Institutes of Health grant 1U24CA18092401A1 and the Air Force Office of Scientific Research through grants FA9550-09-1-0172 and FA9550-15-1-0045 and FA9550-16-1-0435. In addition, the work was funded under the NIA grants R01 AG048769 and RF1 AG053991.

## References

- Angenent S, Haker S, Tannenbaum A. Minimizing flows for the monge–kantorovich problem. *SIAM journal on Mathematical Analysis*. 2003; 35(1):61–97.
- Bakker EN, Bacsikai BJ, Arbel-Ornath M, Aldea R, Bedussi B, Morris AW, Weller RO, Carare RO. Lymphatic clearance of the brain: perivascular, paravascular and significance for neurodegenerative diseases. *Cellular and Molecular Neurobiology*. Mar; 2016 36(2):181–194. [PubMed: 26993512]
- Bedussi B, van der Wel NN, de Vos J, van Veen H, Siebes M, VanBavel E, Bakker EN. Paravascular channels, cisterns, and the subarachnoid space in the rat brain: A single compartment with preferential pathways. *Journal of Cerebral Blood Flow & Metabolism*. Jun.2016 : 0271678X16655550.
- Benamou JD. Numerical resolution of an ‘unbalanced’ mass transport problem. *ESAIM: Mathematical Modelling and Numerical Analysis*. 2003; 37(5):851–868.
- Benamou JD, Brenier Y. A computational fluid mechanics solution to the monge-kantorovich mass transfer problem. *Numerische Mathematik*. 2000; 84(3):375–393.
- Carare RO, et al. Solutes, but not cells, drain from the brain parenchyma along basement membranes of capillaries and arteries: significance for cerebral amyloid angiopathy and neuroimmunology. *Neuropathology and applied neurobiology*. 2008; 34(2):131–144. [PubMed: 18208483]
- Chen Y, Georgiou TT, Pavon M. On the relation between optimal transport and schrödinger bridges: A stochastic control viewpoint. *Journal of Optimization Theory and Applications*. 2016; 169(2):671–691.

- Cserr H. Potassium exchange between cerebrospinal fluid, plasma, and brain. *American Journal of Physiology–Legacy Content*. 1965; 209(6):1219–1226.
- De Graaf RA, et al. Differentiation of glucose transport in human brain gray and white matter. *Journal of Cerebral Blood Flow & Metabolism*. 2001; 21(5):483–492. [PubMed: 11333558]
- De Sousa PL, et al. In vivo MRI assessment of a novel GdIII-based contrast agent designed for high magnetic field applications. *Contrast media & molecular imaging*. 2008; 3(2):78–85. [PubMed: 18412106]
- Evans LC. Partial differential equations and Monge-Kantorovich mass transfer. *Current Developments in Mathematics*. 1997:65–126.
- Haber E, Rehman T, Tannenbaum A. An efficient numerical method for the solution of the 1\_2 optimal mass transfer problem. *SIAM Journal on Scientific Computing*. 2010; 32(1):197–211. [PubMed: 21278828]
- Haker S, Zhu L, Tannenbaum A, Angenent S. Optimal mass transport for registration and warping. *International Journal of Computer Vision*. 2004; 60(3):225–240.
- Horn BK, Schunck BG. Determining optical flow. *Artificial Intelligence*. 1981; 17(1-3):185–203.
- Iliff JJ, et al. A paravascular pathway facilitates csf flow through the brain parenchyma and the clearance of interstitial solutes, including amyloid  $\beta$ . *Science Translational Medicine*. 2012; 4(147):147ra111–147ra111.
- Iliff JJ, et al. Brain-wide pathway for waste clearance captured by contrast-enhanced mri. *The Journal of Clinical Investigation*. Mar; 2013a 123(3):1299–1309. [PubMed: 23434588]
- Iliff JJ, et al. Cerebral arterial pulsation drives paravascular csf–interstitial fluid exchange in the murine brain. *The Journal of Neuroscience*. Nov; 2013b 33(46):18 190–18 199.
- Jiang Q, Zhang L, Ding G, Davoodi-Bojd E, Li Q, Li L, Sadry N, Nedergaard M, Chopp M, Zhang Z. Impairment of the glymphatic system after diabetes. *Journal of Cerebral Blood Flow & Metabolism*. Jun.2016 :0271678X16654702.
- Kress BT, et al. Impairment of paravascular clearance pathways in the aging brain. *Annals of neurology*. Dec; 2014 76(6):845–861. [PubMed: 25204284]
- Lee H, et al. The effect of body posture on brain glymphatic transport. *The Journal of Neuroscience*. Aug; 2015 35(31):11 034–11 044.
- Lucas BD, Kanade T, et al. An iterative image registration technique with an application to stereo vision. *IJCAI*. 1981; 81(1):674–679.
- Mueller M, Karasev P, Kolesov I, Tannenbaum A. Optical flow estimation for flame detection in videos. *IEEE Transactions on Image Processing*. Jul; 2013 22(7):2786–2797. [PubMed: 23613042]
- Nedergaard M. Garbage truck of the brain. *Science*. Jun; 2013 340(6140):1529–1530. [PubMed: 23812703]
- Oreškovi D, Klarica M. The formation of cerebrospinal fluid: nearly a hundred years of interpretations and misinterpretations. *Brain research reviews*. 2010; 64(2):241–262. [PubMed: 20435061]
- Otto F. The geometry of dissipative evolution equations: the porous medium equation. *Communications in Partial Differential Equations*. 2001; 26:101–174.
- Pardridge WM. Blood-brain barrier transport mechanisms. *Primer on cerebrovascular diseases*. 1997:21–25.
- Rachev, ST., Rüschendorf, L. *Mass Transportation Problems: Volume I: Theory*. Springer; 1998.
- Ratner, V., Zhu, L., Kolesov, I., Nedergaard, M., Benveniste, H., Tannenbaum, A. Optimal mass transfer based estimation of glymphatic transport in living brain. In: Ourselin, S., Styner, MA., editors. *Proc SPIE 9413*. Mar. 2015
- Tofts, P. *Quantitative MRI of the brain: measuring changes caused by disease*. John Wiley & Sons; 2005.
- Villani, C. *Optimal Transport: Old and New*. Springer; 2008.
- Villani, C. *Topics in Optimal Transportation*. American Mathematical Soc; 2003.
- Wan X, Fu TC, London RE. Charge dependence of the distribution of contrast agents in rat cerebral ventricles. *Magnetic resonance in medicine*. 1992; 27(1):135–141. [PubMed: 1435199]

- Wardlaw JM, Smith C, Dichgans M. Mechanisms of sporadic cerebral small vessel disease: insights from neuroimaging. *The Lancet Neurology*. 2013; 12(5):483–497. [PubMed: 23602162]
- Weller RO, et al. Lymphatic drainage of the brain and the pathophysiology of neurological disease. *Acta neuropathologica*. 2009; 117(1):1–14. [PubMed: 19002474]
- Xie L, et al. Sleep drives metabolite clearance from the adult brain. *Science*. Oct; 2013 342(6156): 373–377. [PubMed: 24136970]
- Zhu, et al. *Stroke: a Journal of Cerebral Circulation*. 2010; 41:2483–2490.

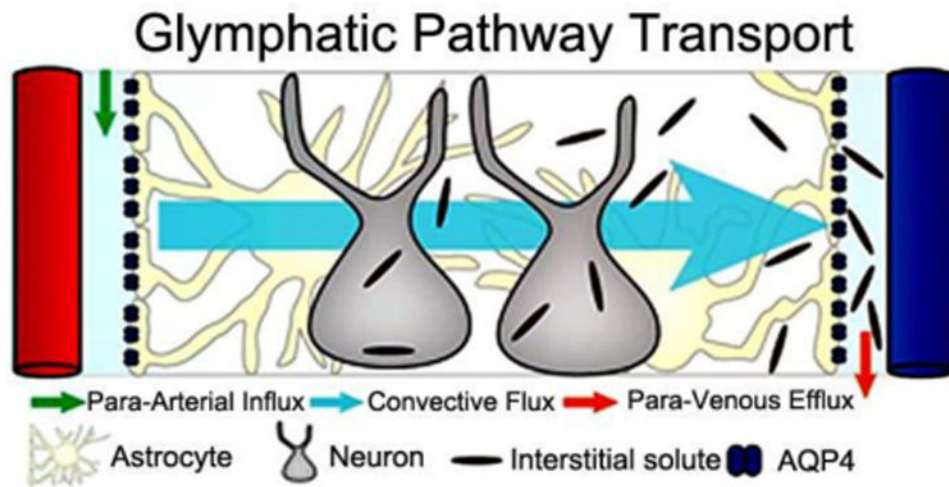


**Figure 1.** Schematic of the glymphatic pathway in rodent brain. Periarterial inflow of cerebrospinal fluid (CSF) enters the brain tissue facilitated by astrocytic endfeet AQP4 water channels; mixes with interstitial fluid and removes the waste products into the peri-venous space.

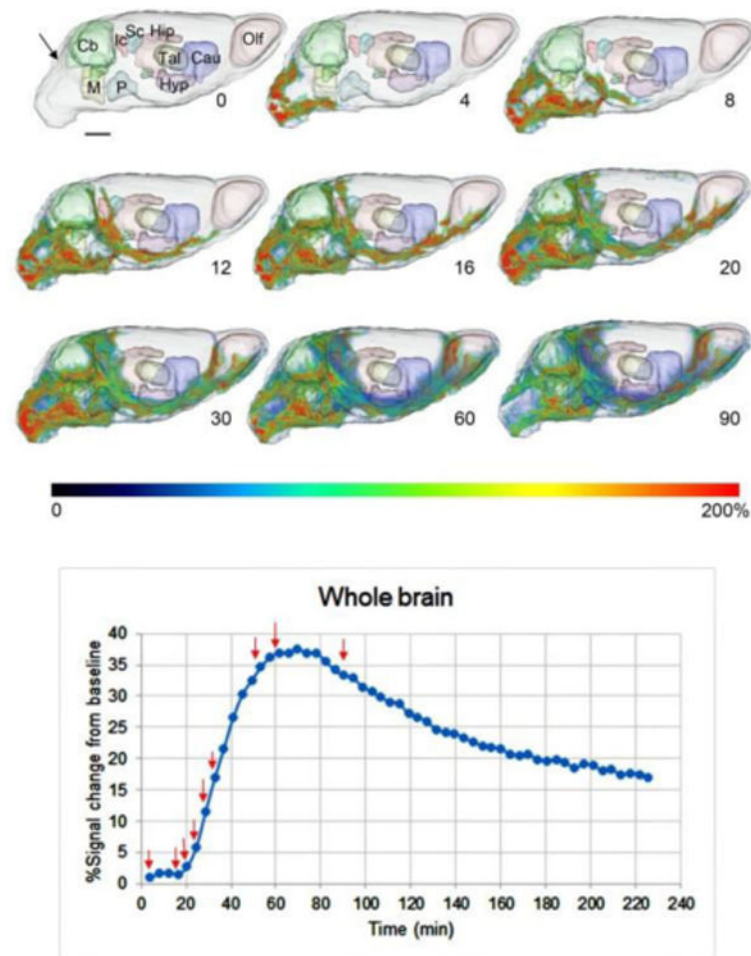


**Figure 2.**

Glymphatic transport of Gd-DTPA in the live rat brain visualized based on a time series of T1-weighted MRI images. The time series show how contrast (represented as a color coded 3D map overlaid on an anatomical template) moves from the cisterna magna (black arrow) into adjacent CSF spaces and into brain parenchyma. The numbers represent the time in min from the start of the CSF contrast infusion. At 12 min contrast is moving into the cerebellum (Cb) and up towards the inferior (Ic) and superior colliculi (sc) and from there slowly penetrating into parenchyma. The corresponding time signal curve is shown below with the red arrows indicating the individual time points captured above. For further details regarding technique and image processing (Iiff et al., 2013a). M=Medulla oblongata; P=Pons; Hip=Hippocampus; Tal=Thalamus; Hyp=Hypothalamus; Cau=Caudate. Color scale: 0 – 200% signal change from baseline.

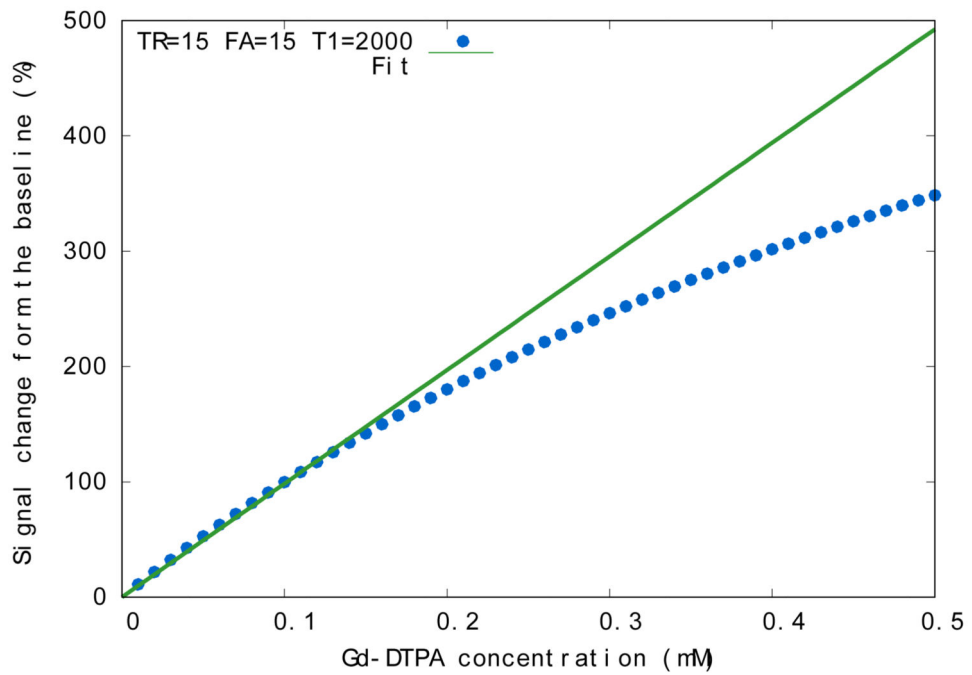


**Figure 3.** Justification of linearity relation between tracer concentration and image brightness (assumption 3).

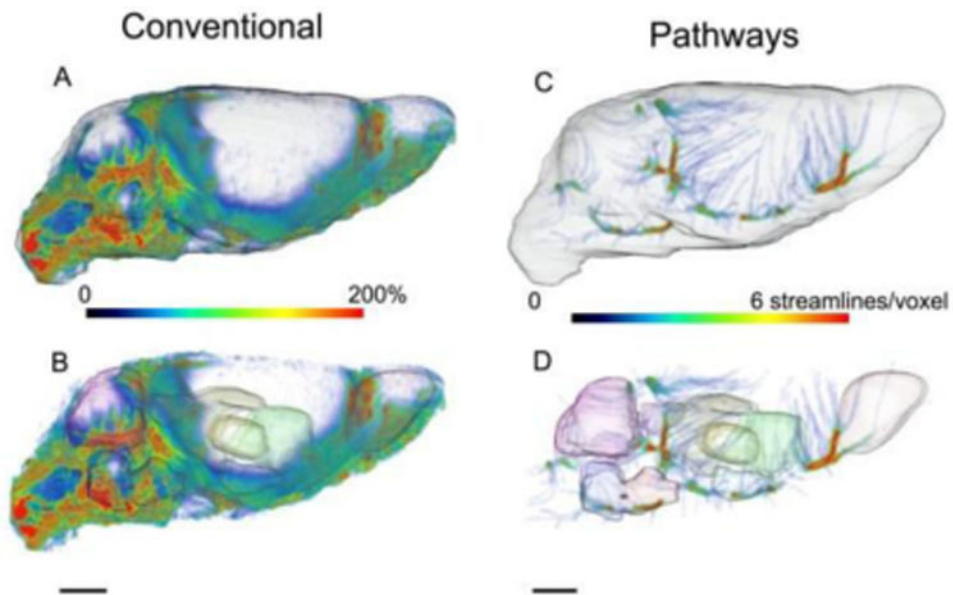


**Figure 4.** Examples of conventional MRI processing versus OMT derived pathways in a rodent brain 40 min after injection of Gd-DTPA into the CSF. (A, B) Glymphatic transport of GD-DTPA after 40 min of circulation and is based on T1-weighted MRIs. The contrast has penetrated into the brain parenchyma in a characteristic pattern. The contrast is represented by a color coded volume rendered map (scale: 0 – 200% signal change from baseline) overlaid on an anatomical volume rendered mask of whole brain and subcortical brain regions. (C) The corresponding OMT defined pathways at the same time point. Specifically, the ‘pathways’ are presented as a color coded map where the red color represents at least 6 crossing streamlines/voxel and blue color 2 – 3 streamlines per voxel. The direction of the physical flow of CSF is from red to blue (for more details see section 5.1). The high streamline density in red is found at the ventral surface of the brain and represents large reservoirs from which several streamlines originate. (D) Shows the same as (C) but overlaid on an anatomical mask of several brain regions including the cerebellum, olfactory bulb, thalamus, caudate, and pons (for anatomical annotations see Fig. 2). Also note that the streamlines (representing smaller reservoirs) originating from the large reservoir are penetrating the brain tissue and appear to be on a trajectory towards the olfactory bulb and surface of the brain. Scale bar = 3 mm.

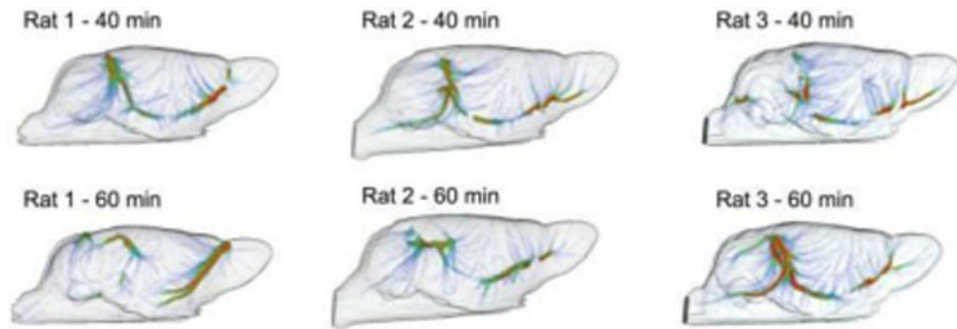


**Figure 5.**

OMT reveals unique brain parenchymal contrast transport conduits. Pathway patterns defined by OMT analysis are shown in three different rats at two time points: 40 min and 60 min after start of Gd-DTPA infusion into CSF. The pathways are represented as color coded volume rendered maps overlaid on a whole brain mask from which the OMT analysis was executed. As can be observed, the pathway trajectories are very consistent from rat to rat. The direction of CSF flow is originating in the ‘red’ reservoirs and towards the ‘blue’ end.

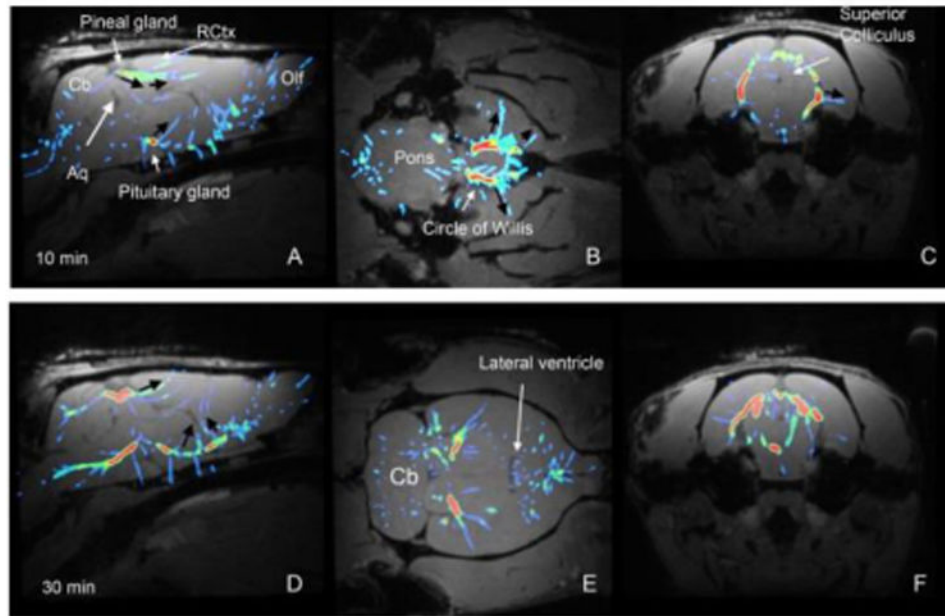


**Figure 6.** Anatomical landmarks in relation to OMT defined transport conduits. (A-C) T1-weighted MRI images of the rat brain in three orthogonal planes with an overlaid color-coded OMT derived pathway map representing 10 – 14 min of CSF circulation of contrast. (D-F) Contrast pathways at 30 min of CSF circulation. As can be seen, the contrast flows along the large arteries at the level of the circle of Willis and up towards the olfactory bulb and the pineal gland. The black arrows indicate flow directions. (C, F) Note the high density pathway at the level of the pineal gland and retrosplenial cortex (RCtx) in agreement with previous studies (Iliff et al., 2013a).

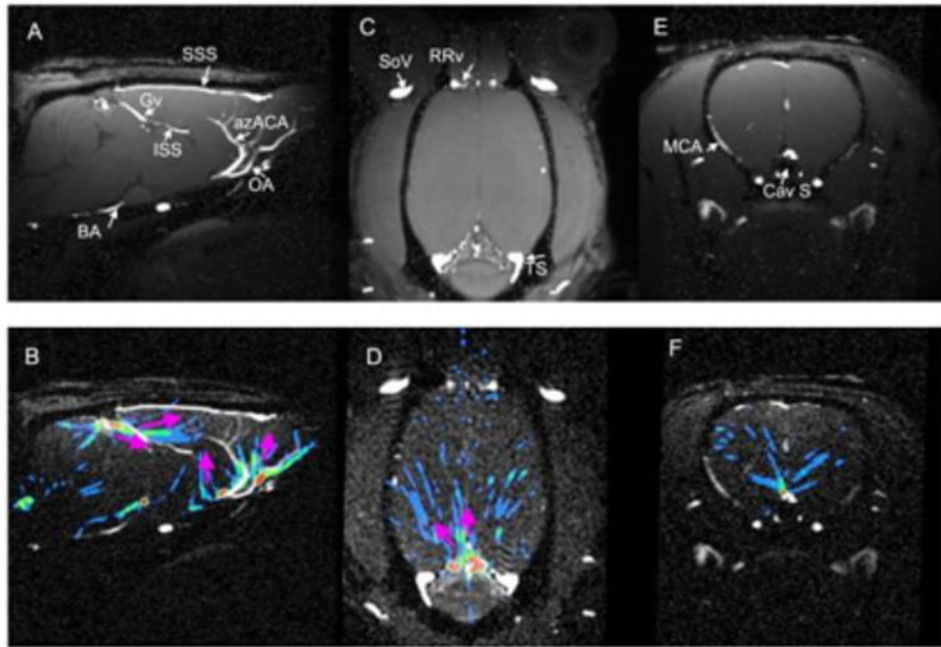


**Figure 7.**

OMT defined transport conduits in relation to large caliber brain vasculature. (A, C, E) represent T1-weighted MRI images in three orthogonal planes from a typical rat brain; the corresponding MR angiographic image is overlaid and the large vasculature is appearing as bright structures. Venous as well as arteries are appearing bright. From anatomical knowledge, the various veins and arteries were identified. (B, D, F) show the OMT defined pathways (40 min) overlaid on the vascular map, and show how the large high density pathways (red and green color) follow the large arteries closely, and the blue pathways (representing smaller reservoirs comprising fewer streamlines/voxel) appear to originate from the large reservoirs associated with the arteries and end towards the venous sinuses or streaming towards them. The flow direction is indicated by the magenta arrows. SSS=superior sagittal sinus; Gv=Galeno vein; ISS=Inferior sagittal sinus; Sov=Supraorbital vein; BA=Basal artery; AzACA=azygos of the anterior cerebral artery; Cav S=Cavernous sinus; OA=olfactory artery; TS=transverse sinus; RRv=rostral rhinal vein.